Electrochemical performance of hybrid supercapacitor device based on birnessite-type manganese oxide decorated on uncapped carbon nanotubes and porous activated carbon nanostructures

F. Ochai-Ejeh[a.b], M.J. Madito[a], K. Makgopa[c], M.N. Rantho[a], O. Olaniyan[a], N. Manyala[a*]

[a]Department of Physics, Institute of Applied Materials, SARChI Chair in Carbon Technology and Materials, University of Pretoria 0028, South Africa.

[b]Department of Physics and Astronomy, University of Nigeria, Nsukka 410001, Nigeria.

[c]Department of Chemistry, Faculty of Science, Tshwane University of Technology, Pretoria 0001, South Africa.

*Corresponding author's email: ncholu.manyala@up.ac.za; faith.ugbo@unn.edu.ng, Tel.: + (27)12 420 3549; Fax: + (27)12 420 2516

Graphical abstract

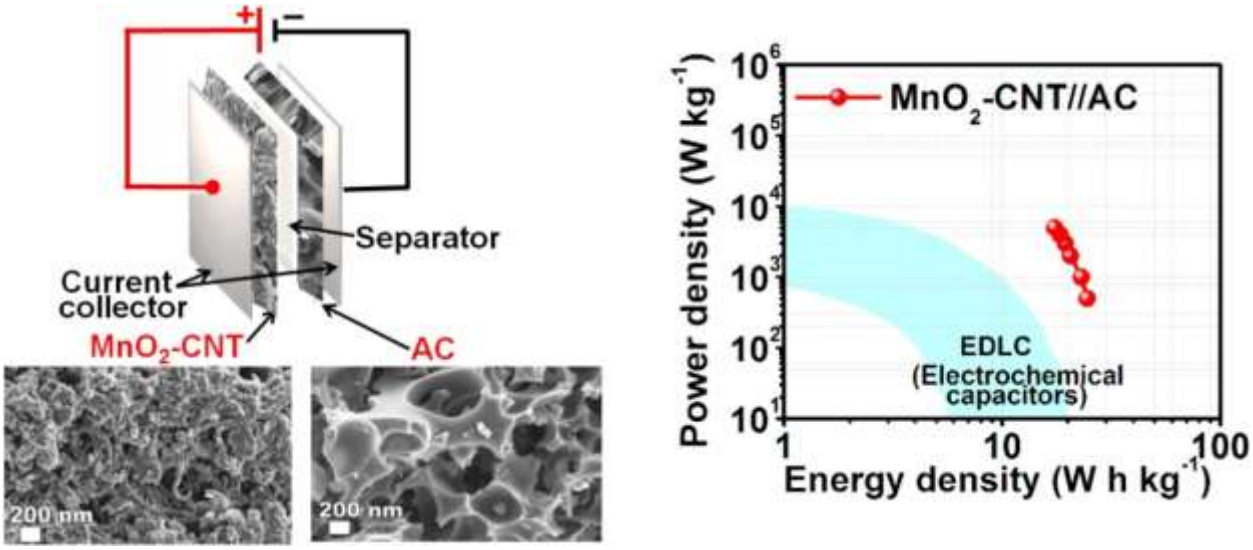

Highlights

- Birnessite-type manganese oxide decorated on uncapped carbon nanotubes was synthesized via facile.
- Activated carbon (AC) was derived from a cork (Quercus Suber).
- A hybrid device was successfully fabricated using MnO_2-CNT as the positive electrode and AC as negative electrode.
- The electrode materials exhibited good electrochemical performance.

ABSTRACT

Birnessite-type MnO_2 synthesized on the surface of carbon nanotubes (CNTs) via facile hydrothermal reflux technique to produce MnO_2-CNT nanocomposite and 3D microporous nanostructured activated carbon (AC) derived from cork (Quercus Suber) with good microstructural, morphological and electrochemical properties are herein reported. A hybrid supercapacitor device comprising of MnO_2-CNT nanocomposite as positive electrode and AC as the negative electrode was successfully fabricated and tested for energy storage application. The device displayed a maximum working potential of up to 2V due to the excellent synergistic contribution from the MnO_2-CNT nanocomposite and AC material derived from cork (Quercus Suber). The fabricated device displayed good electrochemical performance having an energy density of ~25 Wh Kg^{-1} that corresponds to a power density of 500 W Kg^{-1} at a current density of 0.5 A g^{-1} in a 1M Li_2SO_4 aqueous neutral electrolyte. The device exhibited an excellent stability of ~100% coulombic efficiency after 10,000 charge-discharge cycles and excellent capacitance retention after potentiostatic floating test for 60 hours.

KEYWORDS: Birnessite-type MnO_2; activated carbon; hybrid device; reflux synthesis; nanocomposite

1. INTRODUCTION

Electrochemical capacitors (ECs) have gained much research interest due to their excellent properties that display potential promise of meeting the present day global energy needs and have found considerably vast application in systems involving high power density such as lightweight electronic devices (LWEs), hybrid electric vehicles (HEVs.), trams, buses, trains, aircraft and wind turbines [1–7]. ECs mostly known as supercapacitors, are high power density energy storage systems characterized by numerous advantageous properties such as rapid charging-discharging ability, excellent stability and wide operating temperatures etc.. Electrochemical capacitors occupy an intermediary position among the energy storage and conversion systems in such a way that their energy density is higher than that of conventional capacitors but lower than that of lithium-ion batteries (which possess lower power density and are also plagued with poor stability, rapid temperature increase in operative conditions and slow charge-discharge rate) [2,8–10]. Based on their energy storage mechanism electrochemical capacitors (supercapacitors) are classified as the (i) electric double-layer capacitors (EDLCs) and (ii) pseudocapacitors [11–16]. EDLCs utilize an electrochemical double layer capacitance arising from charge separation at the electrode/electrolyte interface (non-faradaic process). In contrary, pseudocapacitors utilize charge-transfer (faradaic processes) occurring on the surface of the electrode material [11–16], and these faradaic processes allow pseudocapacitors to achieve greater capacitances and energy densities compared to EDLCs [14]. Various forms of carbon-based materials such as graphene, carbon nanotubes (CNTs), onion-like carbon (OLC), carbide-derived carbon and activated carbon (AC) have been studied as EDLC electrodes and are mostly utilized as the negative electrode, which is majorly due to their high electrical conductivities, low cost, high surface area, good stability and non-toxicity [1,4,17–21]. Due to the above mentioned excellent properties of carbon-based nanomaterials employed as suitable negative electrode materials in device fabrication for ECs applications, much effort has been devoted on the synthesis of carbon nanomaterials from various renewable and abundant carbon

sources [22–27]. Some of these renewable sources include tree barks [28], seeds [22], leaves [23] nuts shells [29,30]. Recently, activated carbon (AC) obtained from cheap and lightweight material cork (Q. suber), a spongy material which comes from the bark of an evergreen oak tree, has been explored for ECs applications [31,17]. The AC obtained from the cork (Q. suber) exhibited good electrochemical performance, their specific capacitance values was relatively high [32,33] although less than the values resulting from conducting polymers and metal oxides [34,35], their large operating potential window in aqueous neutral electrolyte can be explored for good and synergestic electrochemical cell fabrication. On the other hand, conducting polymers (i.e., polyaniline (PANI), polypyrrole (PPY), etc.) and transition metal oxides/hydroxides (e.g. MnO_2, $Ni(OH)_2$, etc.), including their nanocomposites with EDLC materials, have been employed as positive electrode materials. Among several metal oxides, MnO_2 has been widely researched for ECs application since they are cheap, naturally abundant, environmentally friendly, highly redox-active, possesses a high theoretical capacitance of ~1370 F g^{-1} and displays good performance in aqueous neutral electrolytes than in acidic and alkaline electrolytes [1,4,36,37]. In spite of the good properties displayed by MnO_2, their electrical conductivity is quite low resulting in low cycling stability that compromises their electrochemical performance [1,38]. In order to curb this challenge, carbon nanomaterials with excellent conductivity are used as supports to provide a framework during MnO_2 synthesis [39–42] . Thus, nanocomposites resulting from EDLC materials and manganese oxide-based electrode materials combine electric double layer capacitance of the carbon material and pseudocapacitive charge transfer reactions of the manganese oxide for an improved electrochemical performance [39,40].

Among the EDLC carbon nanomaterials, CNTs are more commonly utilized as support for the growth of metal oxide composite because of its excellent and outstanding intrinsic properties which includes high electrical conductivity (10^4 S cm^{-1}), large surface-to-volume ratio and 1D tubular porous structures which enhance quick ion and electron mobility [1,37,42–44] and functionalizing the CNT material further

increases its surface reactivity and wettability thus making the CNT material more electrolyte accessible thereby increasing the charge storage ability [45]. Several studies on MnO_2–CNT nanocomposites with different morphologies such as nanoflake, nanosheets and nanoflower [4,39,46] have been previously reported, however, only a limited study exists on the tube-like morphology for the MnO_2–CNT nanocomposite. Reports have shown that the tubular morphology displays large surface areas and high surface-to-volume ratio which enhances the flow of electrolyte ions within short diffusion distances [37]. Thus growing MnO_2 on CNT helps to achieve a tubular morphology with the combined advantage of having a large surface-to-volume ratio with short electrolyte diffusion distances, rapid ion transport, improved electrical conductivity and enhanced electrode performance [37].

Briefly, energy density (E_d) of ECs expressed as $E_d = 1/2\,CV^2$, where *C* is the cell specific capacitance and *V* the cell maximum potential [10,31,47,48], largely depends on the cell potential window which is directly dependent on the nature of the electrolyte used as well as the electrode materials used in the cell fabrication [7,49]. Also, the combination of different pseudocapacitive or faradaic redox electrode materials and electric double layer (EDL) materials with different operating potentials in aqueous electrolytes synergistically helps to enhance the energy density of ECs [4,8,10,17,47]. Studies have demonstrated that aqueous neutral electrolytes are able to attain large practical potentials owing to their pH values as compared to acidic and alkaline electrolytes [4,31,36,50–52].

In this report, we present a fabrication of MnO_2-CNT nanocomposite with a tubular morphology that exhibits enhanced electrochemical performance as the positive electrode material with 3D nanostructured AC material obtained from cheap and lightweight material cork (Q. suber) as the negative electrode operating synergistically in 1 M Li_2SO_4 at 2 V in a hybrid (asymmetric) cell device. The EC device displayed excellent stability and improved electrochemical performance after 10 000 charge-discharge cycles.

2. EXPERIMENTAL

2.1 Synthesis of electrode materials

2.1.1 Functionalization of CNTs and Synthesis of MnO_2-CNT

The $KMnO_4$ (Merck, Purity $\geq$ 98%), H_2SO_4 (purity 95 -97 %), H_2O_2 (purity 30 %), HNO_3 (Purity 65 %) reagents were of analytical grade and used without further purification. Deionized water was used throughout for the washing of the synthesized sediments until the final product was achieved. Multi-walled carbon nanotubes (CNTs) (Nanolab, purity: > 94%, length: 5-20 μm and diameter: 10-20 nm), were converted to short and uncapped nanotubes bearing acidic functional groups (mainly: -COOH) prior to their use in the synthesis of the nanocomposite (Scheme 1(a)). Briefly, 0.5 g of pristine CNTs was refluxed for 48 h in 2.6 M HNO_3. The washed deposits of CNTs were sonicated in a mixture of conc. H_2SO_4/HNO_3 (3:1 ratio, 95-97%, and 65% purity, respectively), followed by washing and stirring at 70 ° C for 15 min. in a mixture of H_2SO_4/H_2O_2 (4:1 ratio, 95-97% and 30% purity, respectively). The black powder of CNTs was finally dried at 60 °C overnight after washing. The MnO_2-CNT nanocomposite was synthesized via the conventional hydrothermal reflux technique, as shown in scheme 1(b). Typically, 40 mg of CNTs was dispersed by sonication in 0.02 M $KMnO_4$. Subsequently, the mixture (pH = 7.05) was refluxed at 130 °C in an oil bath for 24 h with continuous magnetic stirring. The resultant dispersion was then centrifuged and washed several times and finally dried at 60 °C overnight in a vacuum oven.

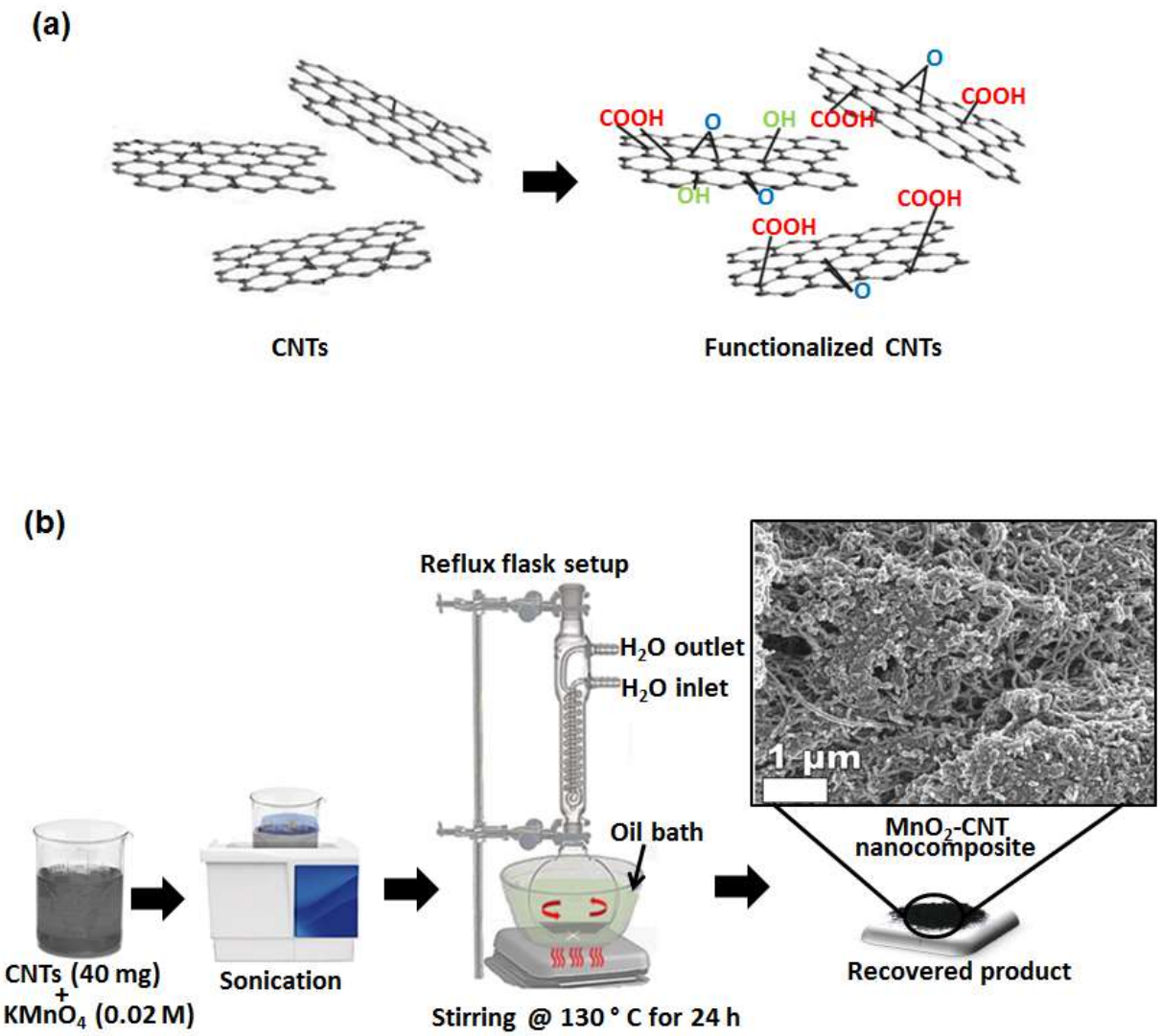

Scheme 1. (a) Schematic view of the chemical structure route from CNTs to functionalized CNTs. (b) Synthesis route for MnO_2-CNT nanocomposite using functionalized CNTs.

2.1.2 Synthesis of AC from Cork (Quercus Suber)

The AC 3D nanostructure material was prepared via a similar procedure in our previous work [31] but with some modification. Briefly, 5 g of cork was crushed and activated with 10 g of KOH and allowed to dry in an oven. The sample was then carbonized in an argon flow at 5 °C/min from room temperature to 850 °C for 2 hours (Scheme 2). The carbonized product was collected and washed with 3 M HCl and deionized water until the filtrate was clear.

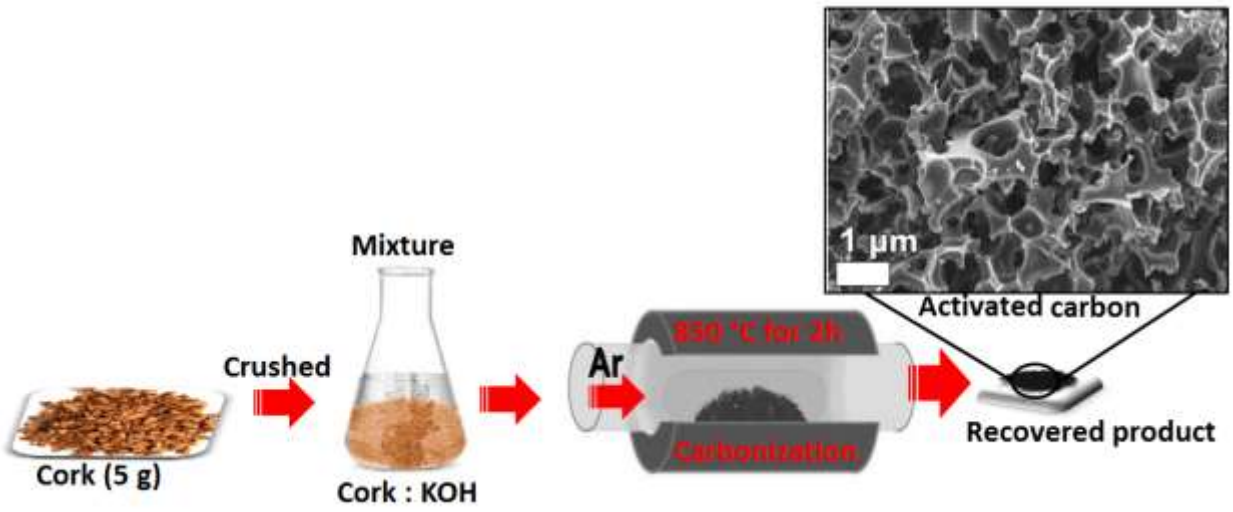

Scheme 2. Synthesis route for 3D nanostructured activated carbon (AC).

2.2 Structural, Morphological, Composition and Electrochemical Characterization

The morphology of the materials were studied via scanning electron microscopy (SEM) using Zeiss ultra plus 55 field emission microscope (FE-SEM) at an accelerating voltage of 2.0 kV. The transmission electron microscopy (TEM) analysis of the samples was carried out in a high-resolution transmission electron microscopy (HR-TEM) JEOL 2100 (from Tokyo Japan) equipped with LaB_6 filament, a Gartan U1000 camera of 2028 x 2028 pixels and operated at 200 kV. The X-ray Diffraction studies of the materials was performed using XPERT-PRO diffractometer (PANalytical Netherlands). Raman analysis was performed using a WiTec alpha 300RAS+ confocal Raman system (WiTecGmbh). X-ray photoelectron spectroscopy (XPS) analysis was performed using Physical Electronics Versaprobe 5000 spectrometer.

The electrochemical characterization of the MnO_2-CNT and AC samples characterization was performed in a three- and two-electrode system using a multi-channel Bio-logic VMP300 potentiostat/galvanostat system at ambient temperature. The MnO_2-CNT electrode for the three-electrode measurement was prepared by thoroughly mixing 80 wt% MnO_2-CNT, 15 wt% carbon black (to enhance the conductivity of

the material), and 5 wt% polyvinyl difluoride (PVDF) binder followed by dropwise addition of 1-methylpyrrolydinone (NMP) in an agate mortar until a uniform paste was obtained. The paste was then coated on 2 cm x 2 cm Nickel foam (NF) and dried in an oven at 60^{o}C for several hours. The AC electrode was similarly prepared and pasted on 2 cm x 2 cm NF. The MnO_2-CNT positive electrode and AC negative electrode materials used in the two electrode measurement were also prepared by the same method but coated on 8 mm radius NFs and dried in an oven at 60 ^{o}C for several hours. The electrodes prepared for the two-electrode measurements were then soaked in 1 M Li_2SO_4 aqueous electrolyte and assembled in a Swagelok cell compartment using a microfiber glass filter paper as a separator. The three-electrode tests were carried out in the 1 M Li_2SO_4 aqueous electrolyte, using Ag/AgCl and glassy carbon as reference and counter electrode respectively. The mass loading for the positive electrode was 1.8 mg and that of the negative electrode was 2.2 mg and total mass of the electrode was 4.0 mg/cm^2. The specific capacitance values of the MnO_2-CNT, AC and MnO_2-CNT//AC hybrid device was determined using equation (1):

$$C_s\,(F\,g^{-1}) = \frac{I\Delta t}{m\Delta U} \quad (1)$$

where *I* (A) is the current, $\Delta t\ (s)$ is the discharge time, *m* is the total mass of the electrodes, ΔU is the maximum potential. The energy density, E_d and the power density, P_d of the MnO_2-CNT//AC hybrid device was calculated using equation (2) and (3) respectively:

$$E_d\ (Wh\ kg^{-1}) = \frac{C_s \Delta U^2}{7.2} \quad (2)$$

$$P_d(WKg^{-1}) = \frac{3.6 \times E_d}{\Delta t} \quad (3)$$

The hybrid device was fabricated taking into consideration the specific capacitance of the MnO_2-CNT and AC electrodes respectively. Since the charge stored in each electrode is:

$$Q = C_s m \Delta U \quad (4)$$

The mass balance equation was adopted to ensure equal charges exists on both electrodes using equation (5):

$$\frac{m_+}{m_-} = \frac{C_{s-}\Delta U_-}{C_{s+}\Delta U_+} \quad (5)$$

The electrochemical impedance spectroscopy measurements were carried out in an open circuit potential in the frequency range of 100 KHz- 10 mHz. Thereafter, the stability tests were performed by continuous charge-discharge for several cycles followed by potentiostatic floating tests at maximum cell potential.

3. RESULTS AND DISCUSSION

3.1 Morphological, structural and compositional characterization

The SEM images of CNT and MnO_2-CNT nanocomposite and AC are presented in Fig. 1. Fig. 1(a) and (b) show the SEM images of the tubular morphologies of CNTs at low and high-magnifications and Fig. 1(c) and (d) display the micrographs of MnO_2-CNT nanocomposites at low and high magnifications. The morphologies show the tube-like nanostructure of the CNT uniformly decorated with MnO_2 nanoparticles. The formation of the MnO_2 on the carbon support can be described by the agglomeration of spherical MnO_2 nanoparticles from the thermal decomposition of $KMnO_4$, which self-assemble from spherical aggregates whose rate of evolution is accelerated by the aging temperature. The presence of the ions of $KMnO_4$ in solution leads to the initial formation of the MnO_2 spherical nanostructures at nucleation points where nanoparticles subsequently formed agglomerate into clusters of spherical nanoparticles as a result of increased surface energies. This can be described by the Ostwald ripening process. The gradual transformation of the spherical aggregates into well-defined MnO_2 tube-like nanostructure is dependent on the specific aging temperatures. This one-dimensional growth process

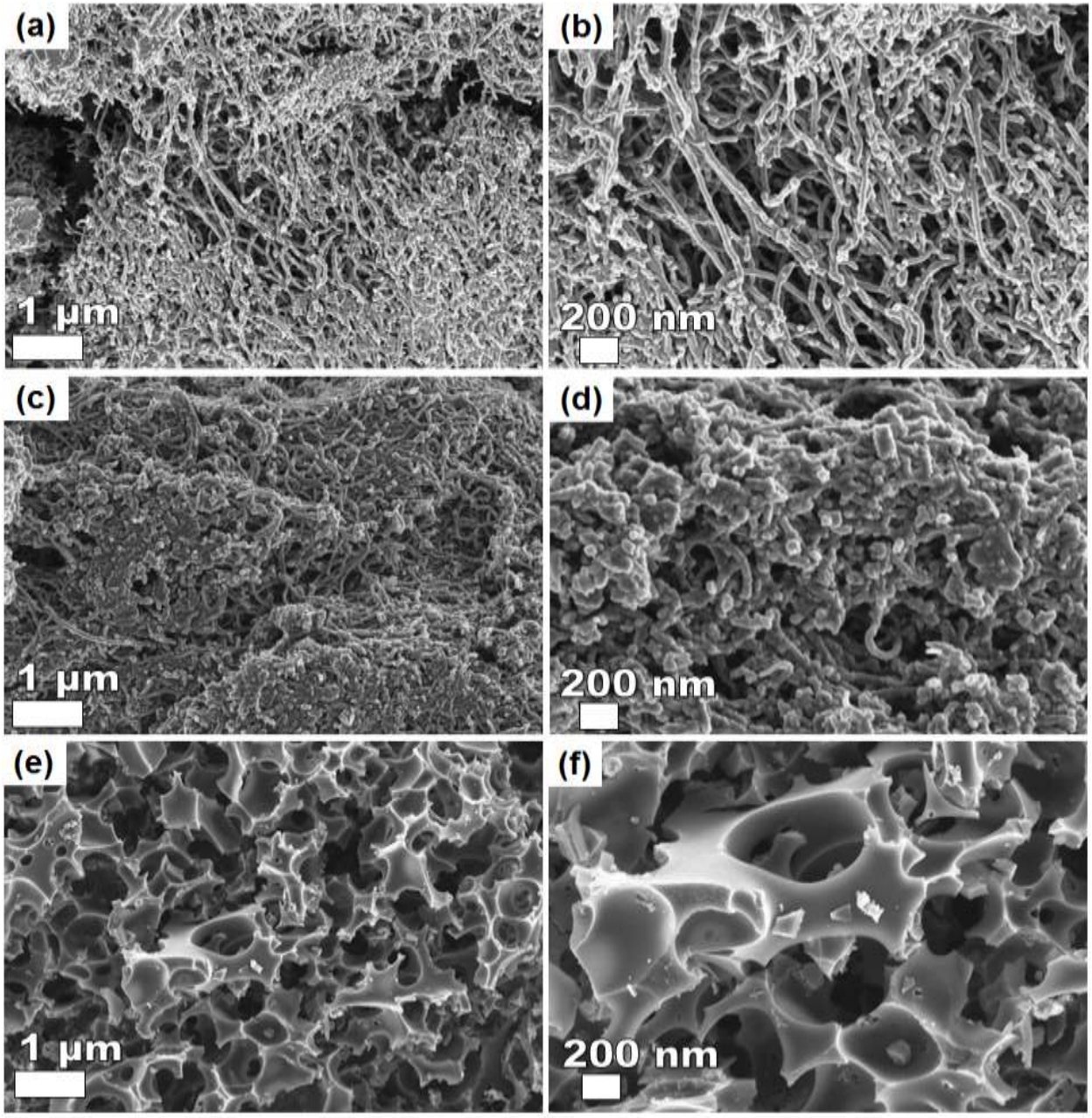

Fig. 1. SEM micrographs of CNT (a) at low and (b) high magnification; of MnO_2-CNT (c) at low and (b) high magnification; and of AC (e) at low and (f) high magnification.

could be as a result of their unique anisotropic characteristic buildup of the nanoparticles [37,39,44]. Fig. 1(e) and (f) display the SEM images of the AC sample at low and high magnification. The micrographs show a 3D interconnected porous network structure. The formation mechanism follows the process of

reduction of KOH by carbon leading to the production of metallic K and K_2CO_3 at >700 °C. K_2CO_3 which decomposes at temperatures ≥ 800 °C, is further reduced by carbon leading to the production of Co_2 and the formation of porous structure.

Fig. 2 compares the TEM images of the CNT and MnO_2-CNT materials which further examine their surface morphology. In Fig. 2(b) and (c), it can be seen that the CNTs are decorated by MnO_2 nanoparticles confirming a successful synthesis of the MnO_2-CNT nanocomposites (nanohybrid) on the surface of the CNTs. These observations corroborate well with the results obtained from the SEM analysis.

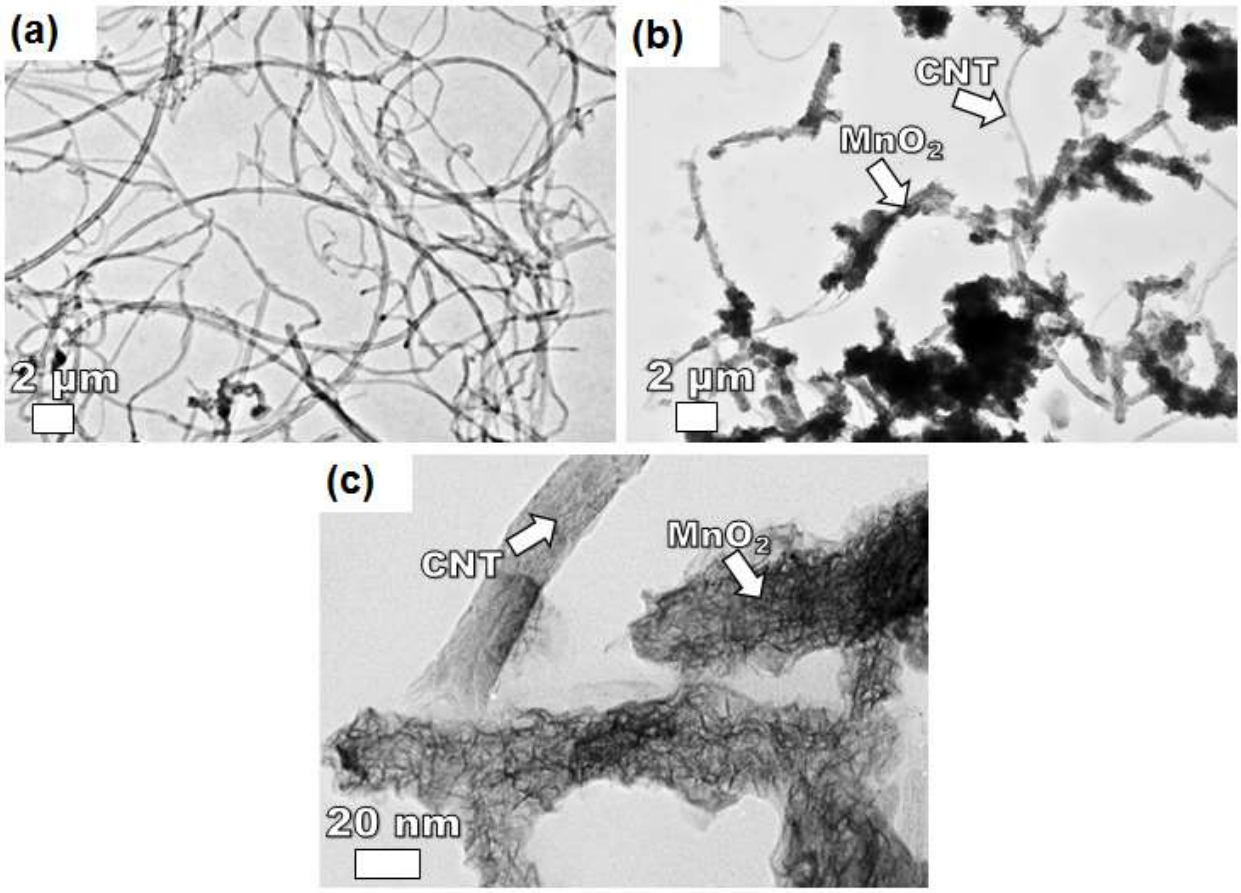

Fig. 2. TEM micrographs of (a) CNT and (b) MnO_2-CNT at low magnification to view the tubular structure of the CNT (c) High-resolution TEM image of MnO_2-CNT.

The structure of the MnO_2-CNT nanocomposite and AC 3D nanomaterial studied by XRD are presented in Fig. 3(a) and (b). The diffraction peaks occurring at 2 theta (^{o}) values of 12^o, 25^o, 37^o and 66^o (Fig. 3(a)) corresponds to the lattice planes of (001), (002), (111) and (020) related to the birnessite-type MnO_2 (PDF #42-1317). The peak observed at 26^o in the CNT spectrum which was also observed in the MnO_2-CNT nanocomposite can be indexed to the (002) plane (PDF #75-1621). The presence of this peak in the MnO_2-CNT nanocomposite is an indication of the presence of carbon in the nanocomposite. The broadening of the diffraction peaks indicates the low crystallinity and/or confirm the nanostructure of the nanocomposite [8,37,46,53]. The XRD pattern of the 3D AC samples shows peaks occurring at 2 theta (^{o}) values of 51^o and 76^o which is related to (100) and (110) lattice planes. The low intensity of the peaks shows poor crystallinity of the as-synthesized 3D AC nanostructure. The structure of the MnO_2-CNT nanocomposite and AC samples was further studied via Raman spectroscopy and the Raman spectra are presented in Fig. 3(c) and (d). The Raman spectrum of MnO_2-CNT nanocomposite (Fig. 3(c)) shows Raman peaks occurring at 495, 570 and 640 cm^{-1} which are in agreement with the three major vibrational features of the birnessite-type MnO_2 compounds, therefore affirming the presence of MnO_2 [54] in the as-synthesized MnO_2-CNT nanocomposite as observed in the XRD results [54]. The presence of CNT in the nanocomposite is signaled by the D and G Raman peaks occurring at ~1346 cm^{-1} and ~1587 cm^{-1} respectively, which are characteristic of the disordered carbon in the sp^2-hybridized carbon network (D-band) and the tangential vibrations of the graphitic carbons (G-band). The D and G peaks which can also be clearly observed in the MnO_2-CNT nanocomposite is an indication of the presence of CNT in the as-synthesized material also confirming the XRD results. In addition, Fig. 3(c) shows the deconvoluted Raman spectra (Lorentzian fit) of the nanocomposite and CNT materials. In the deconvoluted Raman spectra, the D1-mode arises from the defects/disorder present in the carbon lattice structure, the D2-mode from the lattice vibration corresponding to that of the G (G1) mode. These bands, observed in nanocomposite and CNT materials at the same peak positions suggest that the

structure of the CNT material is maintained in the nanocomposite. Furthermore, an evaluation of the ratio of the D to G peak intensities, I_D/I_G shows only a slight increase in the peak ratio value from 0.95 to 0.98 indicating that the structure of the CNT component is not changed in the nanocomposite material. Similar to Fig. 3(c), Fig. 3(d) shows the deconvoluted Raman spectra of AC. The D3-mode arises from the distribution of amorphous carbon in interstitial sites of the disturbed carbon lattice structure while the D4-mode is related to sp^2-sp^3 lattice vibrations. Both of these modes suggest that there exists a level of amorphousness and sp^2-sp^3 bonds within the AC.

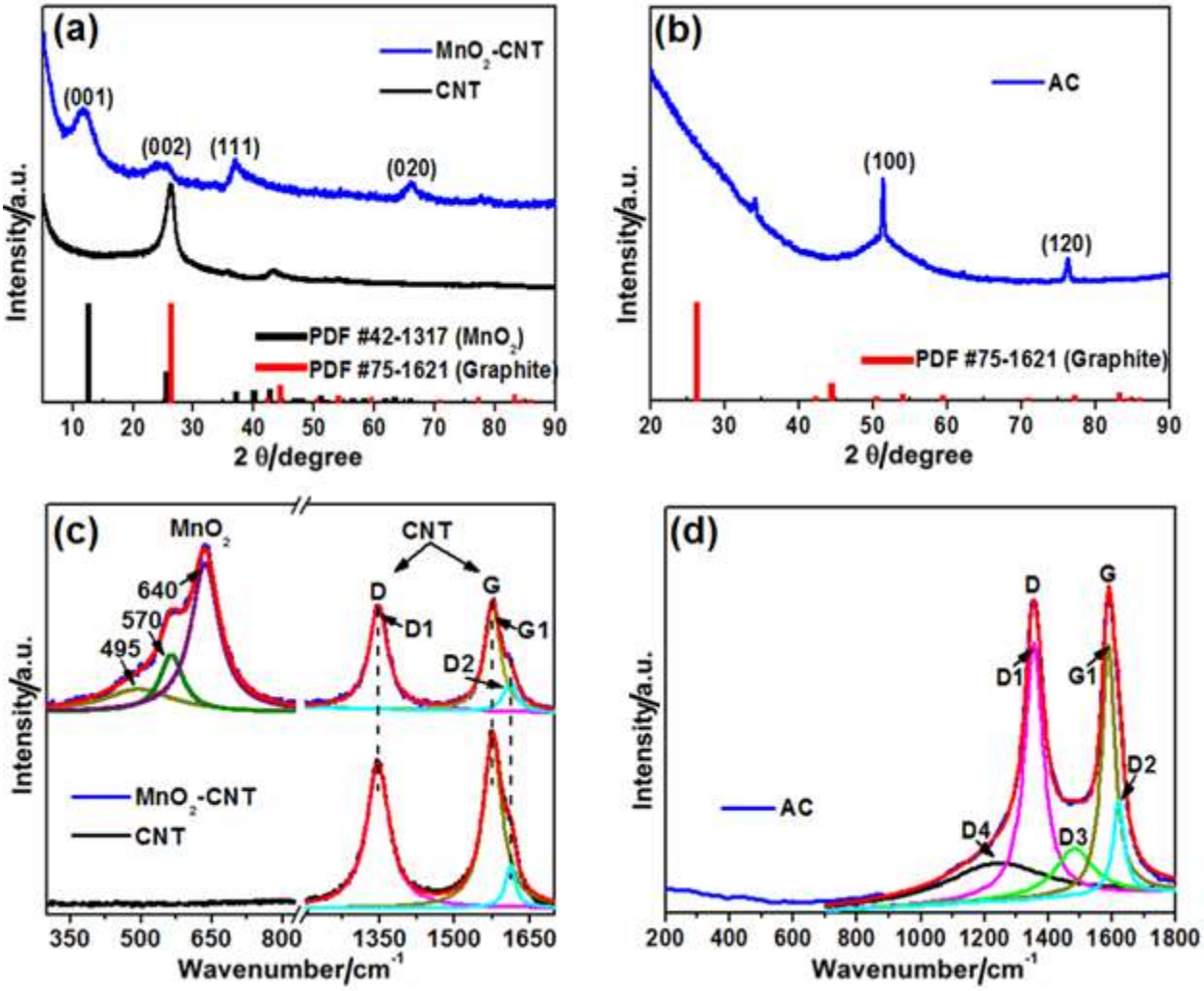

Fig. 3. XRD patterns of (a) MnO_2-CNT, CNT, and (b) of AC. The deconvoluted Raman spectra (Lorentzian fit) of (c) MnO_2-CNT, CNT, and (d) of AC.

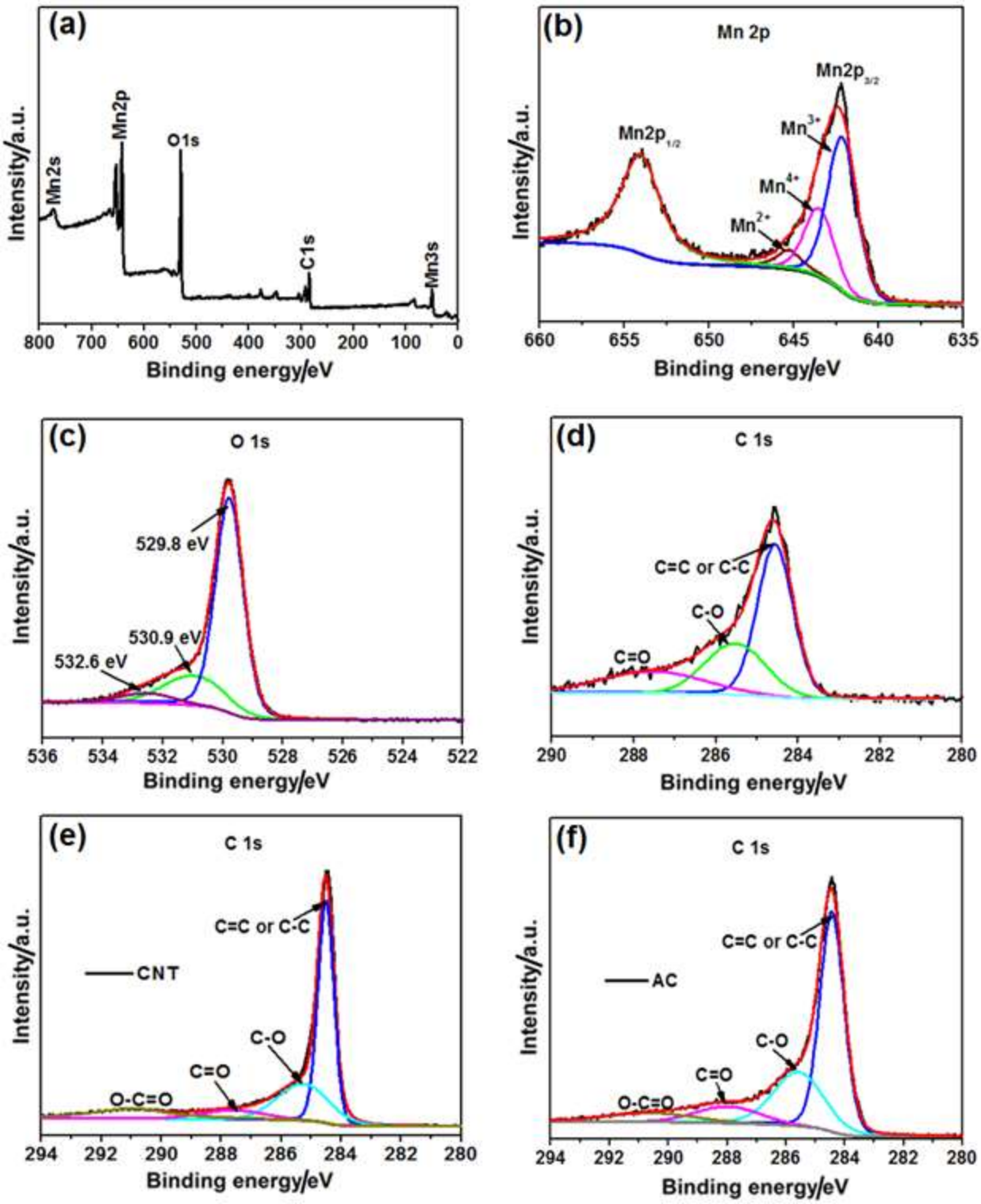

Fig. 4. (a) The wide scan XPS spectra of the as-received MnO_2-CNT nanocomposite material. The core level spectrum of (b) Mn 2p, (c) O 1s and (d) C 1s of the MnO_2-CNT nanocomposite material. The core level spectra of C 1s of the (e) CNT and (f) AC materials.

For further investigation, the samples were analyzed by X-ray photoelectron spectroscopy (XPS) as shown in Fig. 4. The results from Fig. 4(a) shows the wide scan XPS spectrum of the as-received MnO_2-CNT nanocomposite, which displays the main elements (26.98 at% Mn 2p, 45.87 at% O 1s and 27.15 at% C 1s) of the composition of the material. Fig. 4(b) shows the core level spectrum of Mn 2p of the nanocomposite material which reveals the binding energy peaks at 642.5 and 654.1 eV corresponding to Mn $2p_{3/2}$ and Mn $2p_{1/2}$ core levels, respectively. The fitted Mn $2p_{3/2}$ peaks show different Mn oxidation states of the material. Fig. 4(c) shows the core level spectrum of O 1s of the nanocomposite material with fitted peaks at 529.8, 530.9 and 532.6 eV which could be ascribed to Mn–O bonds in the manganese oxide and partly to carbon-oxide components (see Fig. 4(d)). In addition, the core level spectrum of C 1s of the nanocomposite material (Fig. 4(d)) shows the strongest peak at about 284.5 eV attributed to the graphitic carbon, C=C and/or C-C bonds that exist in the CNT, and other peaks at 285.5 and 287.6 eV corresponding to C−O and C=O (carbon-oxide components/functional groups). This is in agreement with the core level spectrum of C 1s of the CNT material which shows the C=C, C−O, C=O and O−C=O components at 284.5, 285.5, 287.6 and 290.3 eV, respectively, as shown in Fig. 4(e). Moreover, the core level spectrum of C 1s of the AC material (Fig. 4(f)) shows similar peaks as the CNT confirming the predominance content of graphitic carbon in the materials.

3.2 Electrochemical characterization

The three-electrode measurements of the MnO_2-CNT nanocomposite and the 3D AC nanostructure measured in 1 M Li_2SO_4 aqueous electrolyte are presented in Fig. 5. A 1 M concentration of Li_2SO_4 aqueous electrolyte is known to be an optimal concentration for high-performance electrochemical capacitors [55]. In carbon-based electrochemical capacitors, dilute solutions (0.1–0.5 mol L^{-1}) of Li_2SO_4 electrolyte have poor conductivity and give poor capacitance, and more concentrated solutions (1.5–2.5 mol L^{-1}) give slightly higher capacitance, however, the charge propagation of the capacitors is not

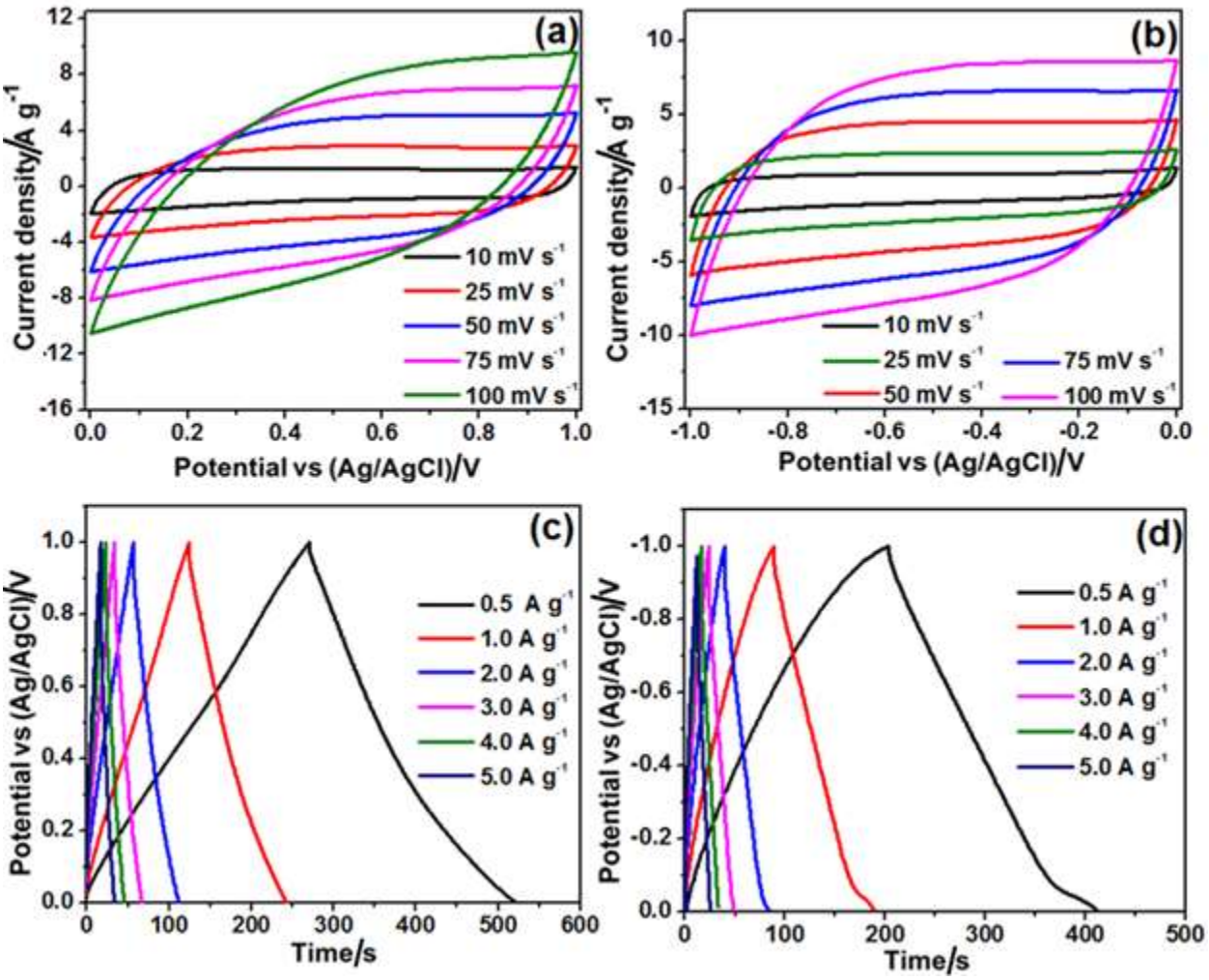

Fig. 5. Cyclic voltammetry curves of (a) MnO_2-CNT and (b) AC. The charge-discharge curves of (c) MnO_2-CNT and (d) AC materials.

adequate, mainly due to sterical hindrance caused by solvated molecule complexes [55]. Fig. 5(a) shows the CV curves of the MnO_2-CNT nanomaterial measured in the potential window of 0.0 - 1.0 V vs. Ag/AgCl at different scan rates from 10 - 100 mV s^{-1}. Symmetric quasi-rectangular and reversible pseudocapacitive CV curves with no redox peaks can be observed which are related to the combined electrochemical behavior of MnO_2 and CNT component of the MnO_2-CNT nanomaterial. Fig. 5(b) displays the CV curves of the AC material performed in the potential window of -1.0 – 0.0 V vs. Ag/AgCl measured at different scan rates of 10 – 100 mV s^{-1}. Nearly rectangular, symmetric CV curves with good

current response are observed which are characteristic of electric double layer capacitive behavior of carbon material. The charge-discharge (GCD) plots of the MnO_2-CNT and AC electrode materials measured at various current densities from 0.5 – 5.0 A g^{-1} are displayed in Fig. 5(c) and (d). The GCD curves display almost linear plots. The specific capacitance of the MnO_2-CNT and AC electrode at 0.5 A g^{-1}, evaluated from equation (1) are 125.5 F g^{-1} and 105 F g^{-1} respectively. Based on the results from the half-cell measurements of the electrode materials, a hybrid electrochemical device, MnO_2-CNT//AC, was fabricated with MnO_2-CNT as the positive electrode and AC as the negative electrode. The charge balance theory (equation (5)) was used to balance up the charges that exist on both electrodes.

The two-electrode measurements of the MnO_2-CNT//AC hybrid electrode device are presented in Fig. 6. Fig. 6(a) shows the respective CV curves of the MnO_2-CNT and AC electrodes in 1 M Li_2SO_4 aqueous electrolyte within the potential window of -1.0 – 1.0 V vs. Ag/AgCl at a scan rate of 25 mV s^{-1}. The comparative CV plots show that the pseudocapacitive and electric double layer characteristic of the MnO_2-CNT and AC electrodes, respectively, can be effectively combined for the fabrication of a hybrid cell device. Both electrodes displayed good current response with good stability within their respective operating potential windows. Therefore, from this observation, it is expected that the hybrid cell device should operate excellently within the combined potential windows of both electrode materials leading to the enhanced energy densities [8,17,39]. Fig. 6(b) illustrates the CV curves of the hybrid cell at different operating potentials from 1.6 – 2.0 V showing that the hybrid electrode indeed is able to operate within the extended potential window of up to 2.0 V as observed by the behavior of the half-cell (three electrode) analysis. This excellent increase in the operating window of the hybrid (asymmetric) device is also assisted by the use of the neutral electrolytes, that are able to operate with large operating potential windows due to their excellent ion solvation, pH and the over-potential for the hydrogen evolution [31,52]. The CV curves of the MnO_2-CNT//AC hybrid cell device at various scan rates ranging from 10 – 100 mV s^{-1} is presented in Fig. 6(c). Rectangular CV curves related to an ideal

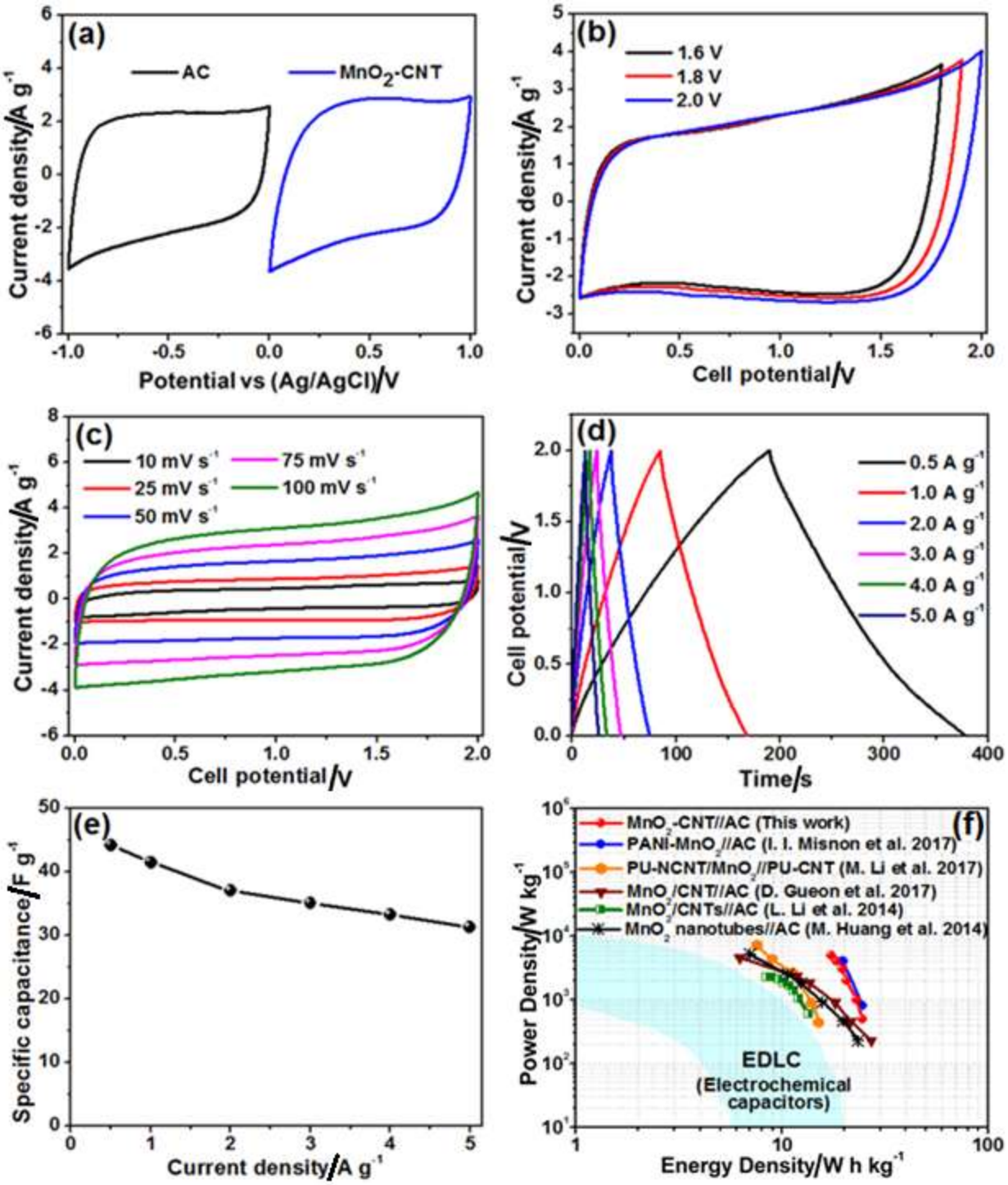

Fig. 6. (a) CV curves of MnO_2-CNT and AC at 25 mV s^{-1}, (b) CV plots of hybrid Cell of MnO2-CNT//AC at 25 mV s^{-1} at various potential windows in 1 M Li_2SO_4, (c) CV plots of MnO_2-CNT//AC ranging from 10 mV s^{-1} - 100 mV s^{-1}, (d) CD plots of MnO_2-CNT//AC ranging from 0.5 A g^{-1}, - 5.0 A g^{-1}, (e) Plot of specific capacitance as a function of current density and (f) Ragone plot of the cell with comparison to similar work in the literature

capacitive electrode is observed for the MnO_2-CNT//AC hybrid device in the potential window of 0 - 2.0 V. The rectangular shape of the CV curves are still maintained even as the scan rate is increased to 100 mV s^{-1} which is an indication of the good capacitive behavior of the hybrid electrode. Fig. 6(d) displays the GCD plots of the hybrid cell carried out at various current densities of 0.5 - 5.0 A g^{-1}. The specific capacitance of the hybrid cell ranges from 44.25 – 31.25 F g^{-1} at 0.5 – 5.0 A g^{-1} (taking into consideration the total mass of the electrodes). The device displayed retention of over 70% of the specific capacitance value at the high current density of 5.0 A g^{-1}. The plot of specific capacitance vs. current density is presented in Fig. 6(e). An energy density value of 24.58 Wh kg^{-1} corresponding to a power density of 500 W Kg^{-1} was obtained from the hybrid device. The Ragone plot of the MnO_2-CNT//AC that is a plot of power density vs. energy density is as shown in figure 6(f). The energy density value obtained from this device is superior or comparable to similar hybrid device electrodes reported earlier in literature, as shown in the Ragone plot and table 1. Table 1 is a comparison of this work with works earlier reported.

Table 1. Electrochemical performance comparison of hybrid cell devices of this work and works earlier reported.

Electrode device	**Electrolyte**	**Current density (A g^{-1})**	**Potential window (V)**	**Energy density (Wh kg^{-1})**	**Power density (W Kg^{-1})**	**Ref.**
MnO_2CNT//AC	0.5 M Na_2SO_4	1.0	2.0	13.9	-	[4]
MnO_2//AC	1 M Na_2SO_4	0.1	2.0	17.1	100	[8]
PU-NCNT/MnO_2//PU-CNT	1 M Na_1SO_4	1.0	1.8	14.76	7211	[46]
MnO_2/CNT//AC	2 M KNO_3	0.1	2.0	21.0	123	[67]
MnO_2/CNT//AC	1 M Na_2SO_4	0.25	1.8	27.0	225	[39]
MnO_2 nanotubes//AC	1 M Na_2SO_4	0.25	1.8	22.5	146200	[37]
PANI-MnO_2//AC	6 M KOH	0.5	1.6	20	400	[68]
MnO_2/CNT//AC	1 M Na_2SO_4	1.0	1.5	13.3	600	[1]
MnO_2//AC	0.1 M K_2SO_4	0.55	2.2	17.3	605	[69]
MnO_2//AC	0.5 M K_2SO_4	-	1.8	28.4	150	[70]
Graphene/MnO_2//Graphene	1 M Na_2SO_4	5.0	2.0	7.0	5000	[71]
Graphene/MnO_2//AC nanofiber	1 M Na_2SO_4	-	1.8	51.1*	102.2*	[72]
MnO_2//Graphene hydrogel	0.5 M Na_2SO_4	1.0	2.0	23.2	1000	[73]
Graphene/MnO_2//Graphene/Ag	1 M Na_2SO_4	-	1.8	50.8*	101*	[74]
MnO_2//rGO flexible solid device	PVA/H_3PO_4 gel	0.2	0.7	17	2520	[75]
MnO_2-CNT//AC	1 M Li_2SO_4	0.5	2.0	24.58	500	This work

*Calculated from the CV curves

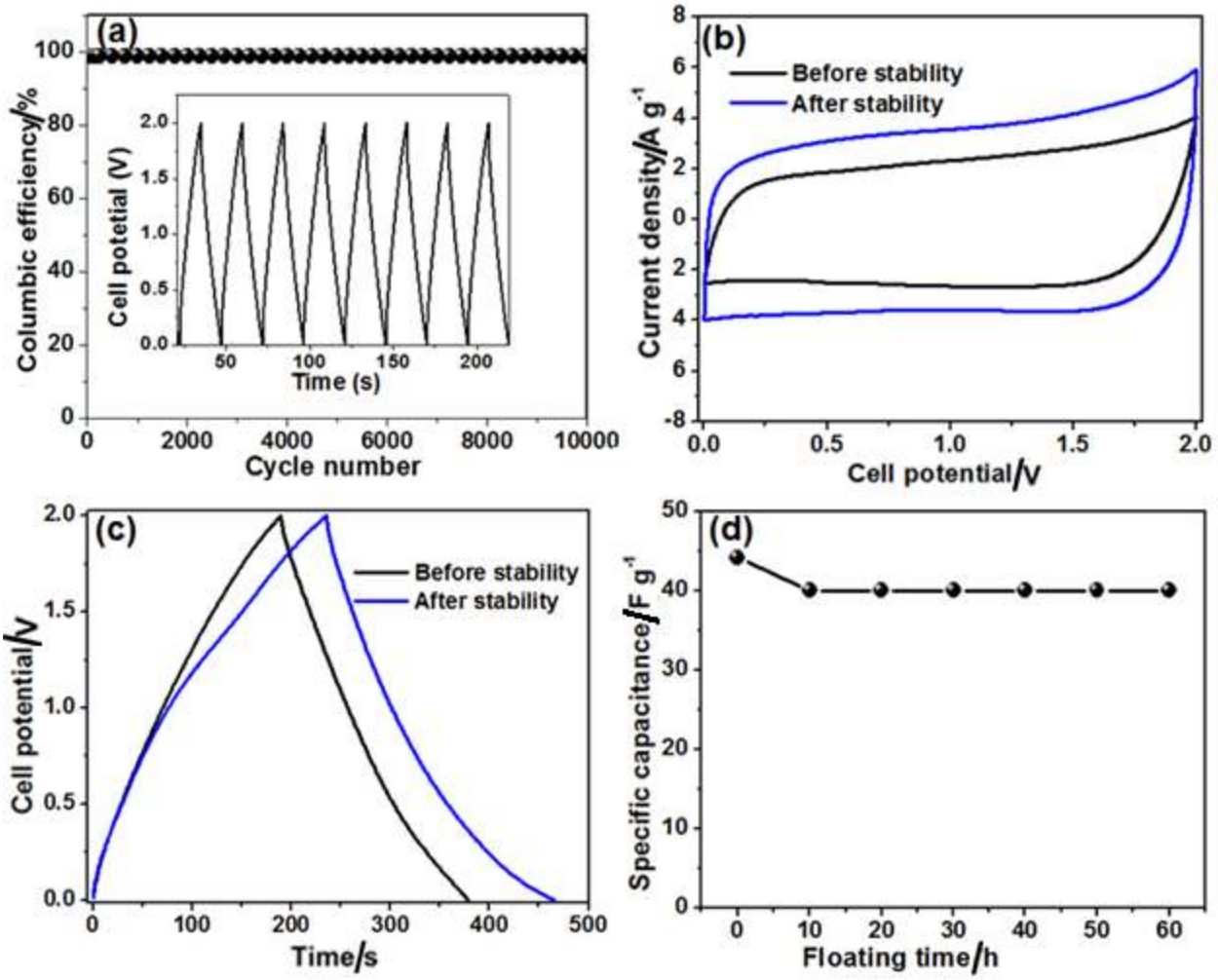

Fig. 7. (a) Plot of columbic efficiency as a function of cycle number, (b) CV curves before and after stability of the MnO_2-CNT//AC hybrid device at 25 mV s^{-1}, (c) CD curves before and after stability of the MnO_2-CNT//AC hybrid device at 0.5 A g^{-1} and (d) Plot of specific capacitance as a function of floating time.

In addition to the high energy density displayed by the hybrid device, it also exhibited excellent stability of ~100% columbic efficiency at up to 10,000 cycles (see Fig. 7(a)). The stability test of a device is important because it shows the electrochemical behavior of the device over a prolonged period [17,56,57]. The remarkable stability performance of this device may be attributed to the presence of the MnO_2-CNT nanocomposite because of their nanotube-like structure which possess high resiliency which is able to accommodate large capacity changes throughout the charge/discharge duration with enhanced effect on the life cycle of the device [58]. Also the synergistic contribution of the 3D porous AC

which provides more accessible pores sites for the diffusion of electrolyte ions [37,59]. This excellent electrode performance is confirmed by the improvement of the capacitance of the hybrid device after 10 000 charge/discharge cycles as depicted in the CV and CD plots shown in Fig. 7(b) and 7(c). The stability of the MnO_2-CNT//AC hybrid device was further tested via potentiostatic floating test at 1.0 A g^{-1} and maximum potential of 2.0 V for 60 hours as it is an adopted reliable technique to accurately evaluate the stability performance of the supercapacitor device. A plot of specific capacitance vs.. floating time for the hybrid device is presented in Fig. 7(d). A decrease in specific capacitance can be observed during the first 10 hours, which stabilized for the rest of the floating time displaying 90% capacitance retention. The stability performance of this device demonstrates the excellent capacitive performance which indicates that the long-term cycling and floating does not significantly affect the stable tube-like/porous structure of the MnO_2-CNT//AC hybrid electrode [17,60].

The electrochemical impedance spectroscopy (EIS) analysis was carried out in an open circuit potential in the frequency range of 10 mHz to 100 kHz. EIS is an important tool for investigating the electron and ion mobility in an electrode material. The MnO_2-CNT//AC hybrid device Nyquist plot is presented in figure 8(a). The intersection of the semicircle and the real *Z'*-axis, indicates the solution resistance (R_S) with the value of 1.2 Ω (see inset to Fig. 8(a)). In the high to middle frequency region, the diameter of the semicircle (inset to Fig. 8(a)), shows the charge transfer resistance (R_{ct}) with the value of 1.0 Ω. Nearly vertical lines parallel to the *y*-axis close to the low frequency region can be observed indicating ideal capacitive behavior of the hybrid electrode device. The equivalent circuit and fitting for the Nyquist plot is presented in Fig. 8(b) and the parameters for fitting are listed in table 2. In the equivalent circuit (inset to Fig. 8(b)), the solution resistance is connected in series with the constant phase element (Q) which is connected in parallel to $R_{ct.}$ The constant phase element Q is given by $Q = 1/T(j\omega)^n$, where T is the frequency independent constant with dimensions of (F $cm^{-2})^n$ (n value is calculated from the slope of the log Z versus log f and ranges from -1 to 1) [61]. For n = -1, n = 0 and n = 1, Q acts as an inductor, pure

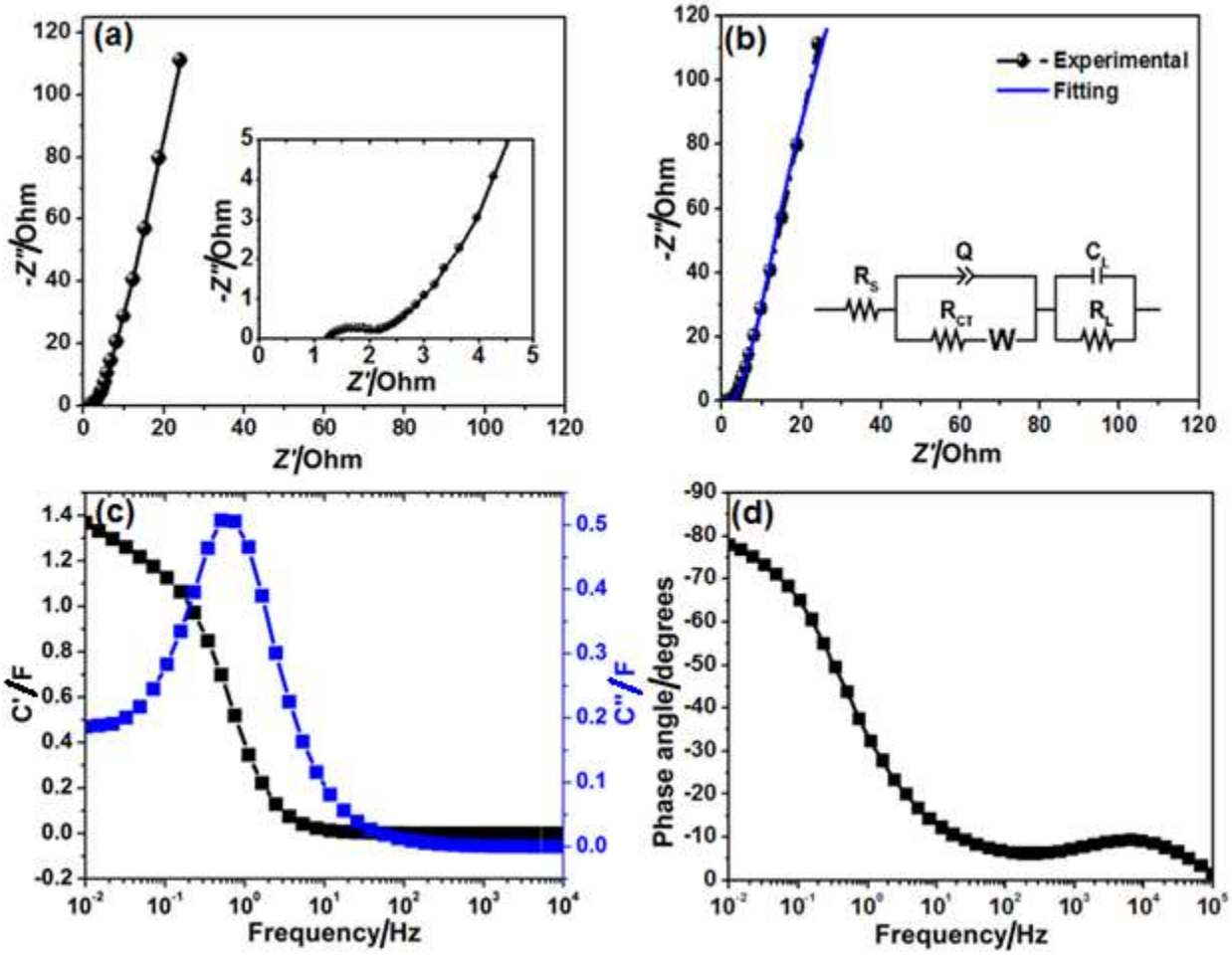

Fig. 8. (a) Nyquist plot of MnO_2-CNT//AC hybrid device, (b) Nyquist plot with fitting by the equivalent circuit inset to the Fig., (c) plot of real and imaginary capacitances as a function of frequency and (d) plot of phase angle as a function of frequency.

resistor and capacitor, respectively [62]. The Warburg diffusion element (*W*) which models the transition from the high to low-frequency region is connected in series with the R_{ct}. These are then connected in series with the mass capacitance (C_L). In an ideal capacitive electrode, this mass capacitance should give rise to a straight line parallel to the *y*-axis but a deviation from the ideal behavior was observed as seen in Fig. 8(a). This deviation is as a result of the resistive element, R_L which is a leakage current connected in parallel to C_L [63,64]. Briefly, in table 2, the small values of the R_S (1.2 Ω) and R_{ct} (1.0 Ω) reveal that the electrodes have a lower diffusion resistance and charge-transfer resistance. The C_L value of 1.1 (i.e.

≈1) denotes the mass capacitance which could be predominantly due to the pseudocapacitive characteristic of the MnO_2-CNT electrode [65]. The *n*-value of 0.9 (i.e. ≈1) with a corresponding low *Q*-value of 0.3 indicates a capacitive behavior (less deviation from an ideal capacitive behavior) of the electrodes. The real (*C'*) and imaginary (*C"*) parts of the capacitance as a function of frequency are presented in Fig. 8(c). *C'* is the real attainable capacitance of the hybrid device with a value of 1.2 F corresponding to a frequency value of 0.01 Hz. *C"* which indicates the transition frequency between an ideal capacitive and ideal resistive behavior [66] of the hybrid device is represented by the peak which occurs at a maximum frequency value of ~0.16 Hz corresponding to a relaxation time, τ of ~6.3 s, evaluated from $\tau = {}^{1}/_{\omega_{max}} = {}^{1}/_{2\pi f_{max}}$. The phase angle of the hybrid device is -78° which is close to the ideal value of -90° indicating good capacitive behavior.

Table 2. The equivalent circuit fitting parameters for the Nyquist plot of the MnO_2-CNT//AC hybrid device.

Device electrodes	**Fitting parameters for the Nyquist plot**				
	R_S **(Ω)**	R_{ct} **(Ω)**	C_L **(F)**	***n***	***Q***
MnO_2-CNT//AC	1.2	1.0	1.1	0.9	0.3

4. CONCLUSION

This work has investigated the electrochemical pseudocapacitive performance of MnO_2-CNT as the positive electrode and AC derived from the cork (Quercus Suber) as the negative electrode in a successfully fabricated MnO_2-CNT//AC device. The MnO_2-CNT nanocomposite and 3D nanostructured activated carbon displayed excellent properties that resulted in good microstructural, morphological and electrochemical properties. The synergistic effects of the MnO_2-CNT and the 3D microporous AC material were maximized to increase the working potential of the hybrid device up to 2.0 V. The device displayed an energy density of ~25 Wh Kg^{-}

^{1} and corresponding power density of 500 W Kg^{-1} at a current density of 0.5 A g^{-1} in 1 M Li_2SO_4 aqueous neutral electrolyte. The device exhibited an excellent stability of ~100% coulombic efficiency after 10, 000 charge-discharge cycles and excellent capacitance retention after potentiostatic floating test for 60 hours. The results obtained suggest that the hybrid device has the potential for high-energy storage device application.

ACKNOWLEDGEMENTS

This research work was supported by the South African Research Chairs Initiative (SARChI) of the Department of Science and Technology and the National Research Foundation (NRF) of South Africa (Grant No. 61056). Any opinion, finding and conclusion or recommendation expressed in this material is that of the author(s) and the NRF does not accept any liability in this regard. Faith O. Ochai-Ejeh acknowledges NRF through SARChI in Carbon Technology and Materials, the Department of Physics at the University of Pretoria, the TETFund through the University of Nigeria for financial support.

REFERENCES

[1] L. Li, Z.A. Hu, N. An, Y.Y. Yang, Z.M. Li, H.Y. Wu, Facile Synthesis of MnO_2 /CNTs Composite for Supercapacitor Electrodes with Long Cycle Stability, J. Phys. Chem. C. 118 (2014) 22865–22872. doi:10.1021/jp505744p.

[2] Electrochemical Capacitor Applications, (2008).

https://www.electrochem.org/dl/interface/spr/spr08/spr08_p53-57.pdf (accessed September 7, 2017).

[3] F.O. Ochai-Ejeh, M.J. Madito, D.Y. Momodu, A.A. Khaleed, O. Olaniyan, N. Manyala, High performance hybrid supercapacitor device based on cobalt manganese layered double hydroxide and activated carbon derived from cork (Quercus Suber), Electrochim. Acta. 252 (2017). doi:10.1016/j.electacta.2017.08.163.

[4] L. Demarconnay, E. Raymundo-Piñero, F. Béguin, Adjustment of electrodes potential window in an asymmetric carbon/MnO2 supercapacitor, J. Power Sources. 196 (2011) 580–586. doi:10.1016/j.jpowsour.2010.06.013.

[5] M. Gidwani, A. Bhagwani, N. Rohra, Supercapacitors: the near Future of Batteries, Int. J. Eng. Invent. 4 (2014) 2278–7461.

[6] P. Simon, Y. Gogotsi, Capacitive Energy Storage in Nanostructured Carbon–Electrolyte Systems, Acc. Chem. Res. 46 (2013) 1094–1103. doi:10.1021/ar200306b.

[7] A. Brandt, S. Pohlmann, A. Varzi, A. Balducci, S. Passerini, Ionic liquids in supercapacitors, MRS Bull. 38 (2013) 554–559. doi:10.1557/mrs.2013.151.

[8] X. Zhang, P. Yu, H. Zhang, D. Zhang, X. Sun, Y. Ma, Rapid hydrothermal synthesis of hierarchical nanostructures assembled from ultrathin birnessite-type MnO2 nanosheets for supercapacitor applications, Electrochim. Acta. 89 (2013) 523–529. doi:10.1016/J.ELECTACTA.2012.11.089.

[9] J.W. Lee, A.S. Hall, J.-D. Kim, T.E. Mallouk, A Facile and Template-Free Hydrothermal

Synthesis of Mn_3O_4 Nanorods on Graphene Sheets for Supercapacitor Electrodes with Long Cycle Stability, Chem. Mater. 24 (2012) 1158–1164. doi:10.1021/cm203697w.

[10] Y. Zhou, H. Xu, N. Lachman, M. Ghaffari, S. Wu, Y. Liu, et al., Advanced asymmetric supercapacitor based on conducting polymer and aligned carbon nanotubes with controlled nanomorphology, Nano Energy. 9 (2014) 176–185.

[11] G. Zhang, M. Kong, Y. Yao, L. Long, M. Yan, One-pot synthesis of γ -MnS / reduced graphene oxide with enhanced performance for aqueous asymmetric supercapacitors, 65402 (n.d.). doi:10.1088/1361-6528/aa52a5.

[12] G. Feng, S. Li, V. Presser, P.T. Cummings, Molecular Insights into Carbon Supercapacitors Based on Room-Temperature Ionic Liquids, J. Phys. Chem. Lett. 4 (2013) 3367–3376. doi:10.1021/jz4014163.

[13] P. Simon, Y. Gogotsi, Materials for electrochemical capacitors, 7 (2008) 845–854. doi:10.1038/nmat2297.

[14] V. Aravindan, M.V. Reddy, S. Madhavi, S.G. Mhaisalkar, G.V. Subba Rao, B.V.R. Chowdari, Hybrid supercapacitor with nano-TiP2O7 as intercalation electrode, J. Power Sources. 196 (2011) 8850–8854. doi:10.1016/J.JPOWSOUR.2011.05.074.

[15] M. Harilal, S.G. Krishnan, B.L. Vijayan, M. Venkatashamy Reddy, S. Adams, A.R. Barron, et al., Continuous nanobelts of nickel oxide–cobalt oxide hybrid with improved capacitive charge storage properties, Mater. Des. 122 (2017) 376–384. doi:10.1016/J.MATDES.2017.03.024.

[16] S.G. Krishnan, M. Harilal, I.I. Misnon, M.V. Reddy, S. Adams, R. Jose, Effect of processing parameters on the charge storage properties of MgCo2O4 electrodes, Ceram. Int. 43 (2017) 12270–12279. doi:10.1016/J.CERAMINT.2017.06.089.

[17] F.O. Ochai-Ejeh, M.J. Madito, D.Y. Momodu, A.. Khaleed, O. Olaniyan, N. Manyala, High performance hybrid supercapacitor device based on cobalt manganese layered double hydroxide and activated carbon derived from cork (Quercus Suber), Electrochim. Acta. 252 (2017) 41–54. doi:10.1016/j.electacta.2017.08.163.

[18] M. Liang, L. Zhi, Graphene-based electrode materials for rechargeable lithium batteries, J. Mater. Chem. 19 (2009) 5871. doi:10.1039/b901551e.

[19] J.K. Gan, Y.S. Lim, A. Pandikumar, N.M. Huang, H.N. Lim, Graphene/polypyrrole-coated carbon nanofiber core–shell architecture electrode for electrochemical capacitors, RSC Adv. 5 (2015) 12692–12699. doi:10.1039/C4RA14922J.

[20] F. Zhang, T. Zhang, X. Yang, L. Zhang, K. Leng, Y. Huang, et al., A high-performance supercapacitor-battery hybrid energy storage device based on graphene-enhanced electrode materials with ultrahigh energy density, Energy Environ. Sci. 6 (2013) 1623. doi:10.1039/c3ee40509e.

[21] W. Gu, G. Yushin, Review of nanostructured carbon materials for electrochemical capacitor applications : advantages and limitations of activated carbon , carbide-derived carbon , aerogels , carbon nanotubes , onion-like carbon , and graphene, (2013). doi:10.1002/wene.102.

[22] X. Li, W. Xing, S. Zhuo, J. Zhou, F. Li, S.-Z. Qiao, et al., Preparation of capacitor's electrode from sunflower seed shell, Bioresour. Technol. 102 (2011) 1118–1123. doi:10.1016/j.biortech.2010.08.110.

[23] K.S. Sulaiman, A. Mat, A.K. Arof, Activated carbon from coconut leaves for electrical double-layer capacitor, Ionics (Kiel). 22 (2016) 911–918. doi:10.1007/s11581-015-1594-9.

[24] A. Özhan, Ö. Şahin, M.M. Küçük, C. Saka, Preparation and characterization of activated carbon from pine cone by microwave-induced ZnCl2 activation and its effects on the adsorption of methylene blue, Cellulose. 21 (2014) 2457–2467. doi:10.1007/s10570-014-0299-y.

[25] T.-C. Weng, H. Teng, Characterization of high porosity carbon electrodes derived from mesophase pitch for electric double-layer capacitors, J. Electrochem. Soc. 148 (2001) A368--A373.

[26] A. Alonso, V. Ruiz, C. Blanco, R. Santamaría, M. Granda, R. Menéndez, et al., Activated carbon produced from Sasol-Lurgi gasifier pitch and its application as electrodes in supercapacitors, Carbon. 44 (2006) 441–446. doi:10.1016/J.CARBON.2005.09.008.

[27] F. Barzegar, A. Bello, D. Momodu, M.J. Madito, J. Dangbegnon, N. Manyala, Preparation and characterization of porous carbon from expanded graphite for high energy density supercapacitor in aqueous electrolyte, J. Power Sources. 309 (2016) 245–253. doi:10.1016/j.jpowsour.2016.01.097.

[28] D. Momodu, A. Bello, K. Oyedotun, F. Ochai-Ejeh, J. Dangbegnon, M. Madito, et al.,

Enhanced electrochemical response of activated carbon nanostructures from tree-bark biomass waste in polymer-gel active electrolytes, RSC Adv. 7 (2017) 37286–37295. doi:10.1039/C7RA05810A.

[29] F. Barzegar, A.A. Khaleed, F.U. Ugbo, K.O. Oyeniran, D.Y. Momodu, A. Bello, et al., Cycling and floating performance of symmetric supercapacitor derived from coconut shell biomass, AIP Adv. 6 (2016) 115306. doi:10.1063/1.4967348.

[30] J. Xu, Q. Gao, Y. Zhang, Y. Tan, W. Tian, L. Zhu, et al., Preparing two-dimensional microporous carbon from Pistachio nutshell with high areal capacitance as supercapacitor materials, Sci. Rep. 4 (2014) 845–854. doi:10.1038/srep05545.

[31] F.O. Ochai-Ejeh, A. Bello, J. Dangbegnon, A.A. Khaleed, M.J. Madito, F. Bazegar, et al., High electrochemical performance of hierarchical porous activated carbon derived from lightweight cork (Quercus suber), J. Mater. Sci. 52 (2017) 10600–10613. doi:10.1007/s10853-017-1205-4.

[32] S.R. Sivakkumar, J.M. Ko, D.Y. Kim, B.C. Kim, G.G. Wallace, Performance evaluation of CNT/polypyrrole/MnO2 composite electrodes for electrochemical capacitors, Electrochim. Acta. 52 (2007) 7377–7385. doi:10.1016/j.electacta.2007.06.023.

[33] A. Bello, F. Barzegar, M.J. Madito, D.Y. Momodu, A.A. Khaleed, T.M. Masikhwa, et al., Electrochemical performance of polypyrrole derived porous activated carbon-based symmetric supercapacitors in various electrolytes, RSC Adv. 6 (2016) 68141–68149. doi:10.1039/C6RA12690A.

[34] K. Liang, T. Gu, Z. Cao, X. Tang, W. Hu, B. Wei, In situ synthesis of SWNTs@MnO2/polypyrrole hybrid film as binder-free supercapacitor electrode, Nano Energy. 9 (2014) 245–251. doi:10.1016/j.nanoen.2014.07.017.

[35] X. Cai, S. Hua, C. Kok, L. Lai, J. Lin, Z. Shen, High-performance asymmetric pseudocapacitor cell based on cobalt hydroxide / graphene and polypyrrole / graphene electrodes, J. Power Sources. 275 (2015) 298–304. doi:10.1016/j.jpowsour.2014.10.204.

[36] T. Brousse, P.L. Taberna, O. Crosnier, R. Dugas, P. Guillemet, Y. Scudeller, et al., Long-term cycling behavior of asymmetric activated carbon/MnO2 aqueous electrochemical supercapacitor, J. Power Sources. 173 (2007) 633–641. doi:10.1016/j.jpowsour.2007.04.074.

[37] M. Huang, Y. Zhang, F. Li, L. Zhang, R.S. Ruoff, Z. Wen, et al., Self-assembly of mesoporous nanotubes assembled from interwoven ultrathin birnessite-type MnO2 nanosheets for asymmetric supercapacitors., Sci. Rep. 4 (2014) 3878. doi:10.1038/srep03878.

[38] Y. Jin, H. Chen, M. Chen, N. Liu, Q. Li, Graphene-Patched CNT/MnO_2 Nanocomposite Papers for the Electrode of High-Performance Flexible Asymmetric Supercapacitors, ACS Appl. Mater. Interfaces. 5 (2013) 3408–3416. doi:10.1021/am400457x.

[39] D. Gueon, J.H. Moon, MnO_2 Nanoflake-Shelled Carbon Nanotube Particles for High-Performance Supercapacitors, ACS Sustain. Chem. Eng. 5 (2017) 2445–2453. doi:10.1021/acssuschemeng.6b02803.

[40] B. Brown, I.A. Cordova, C.B. Parker, B.R. Stoner, J.T. Glass, Optimization of Active Manganese Oxide Electrodeposits Using Graphenated Carbon Nanotube Electrodes for Supercapacitors, Chem. Mater. 27 (2015) 2430–2438. doi:10.1021/cm504519m.

[41] J. Jiang, Y. Li, J. Liu, X. Huang, C. Yuan, X.W.D. Lou, Recent Advances in Metal Oxide-based Electrode Architecture Design for Electrochemical Energy Storage, Adv. Mater. 24 (2012) 5166–5180. doi:10.1002/adma.201202146.

[42] G. Lota, K. Fic, E. Frackowiak, Carbon nanotubes and their composites in electrochemical applications, Energy Environ. Sci. 4 (2011) 1592. doi:10.1039/c0ee00470g.

[43] H. Jiang, P.S. Lee, C. Li, 3D carbon based nanostructures for advanced supercapacitors, Energy Environ. Sci. 6 (2013) 41–53. doi:10.1039/C2EE23284G.

[44] S.C. Pang, S.F. Chin, C.Y. Ling, Controlled Synthesis of Manganese Dioxide Nanostructures via a Facile Hydrothermal Route, J. Nanomater. 2012 (2012) 1–7. doi:10.1155/2012/607870.

[45] G. Xiong, C. Meng, R.G. Reifenberger, P.P. Irazoqui, T.S. Fisher, Graphitic Petal Micro-Supercapacitor Electrodes for Ultra-High Power Density, Energy Technol. 2 (2014) 897–905. doi:10.1002/ente.201402055.

[46] Ultrathin manganese dioxide nanosheets grown on partially unzipped nitrogen-doped carbon nanotubes for high-performance asymmetric supercapacitors, J. Alloys Compd. 702 (2017) 236–243. doi:10.1016/J.JALLCOM.2017.01.244.

[47] W.G. Pell, B.E. Conway, Peculiarities and requirements of asymmetric capacitor devices

based on combination of capacitor and battery-type electrodes, J. Power Sources. 136 (2004) 334–345. doi:10.1016/j.jpowsour.2004.03.021.

[48] B.G. Choi, M. Yang, W.H. Hong, J.W. Choi, Y.S. Huh, 3D Macroporous Graphene Frameworks for Supercapacitors with High Energy and Power Densities, ACS Nano. 6 (2012) 4020–4028. doi:10.1021/nn3003345.

[49] C. Zhong, Y. Deng, W. Hu, J. Qiao, L. Zhang, J. Zhang, A review of electrolyte materials and compositions for electrochemical supercapacitors., Chem. Soc. Rev. 44 (2015) 7484–7539. doi:10.1039/c5cs00303b.

[50] F. Béguin, V. Presser, A. Balducci, E. Frackowiak, Carbons and electrolytes for advanced supercapacitors., Adv. Mater. 26 (2014) 2219–51, 2283. doi:10.1002/adma.201304137.

[51] A. Bello, F. Barzegar, M.J. Madito, D.Y. Momodu, A.A. Khaleed, T.M. Masikhwa, et al., Stability studies of polypyrole- derived carbon based symmetric supercapacitor via potentiostatic floating test, Electrochim. Acta. 213 (2016) 107–114. doi:10.1016/j.electacta.2016.06.151.

[52] L. Demarconnay, E. Raymundo-Piñero, F. Béguin, A symmetric carbon/carbon supercapacitor operating at 1.6 V by using a neutral aqueous solution, Electrochem. Commun. 12 (2010) 1275–1278. doi:10.1016/j.elecom.2010.06.036.

[53] K. Makgopa, P.M. Ejikeme, C.J. Jafta, K. Raju, M. Zeiger, V. Presser, et al., A high-rate aqueous symmetric pseudocapacitor based on highly graphitized onion-like carbon/birnessite-type manganese oxide nanohybrids, J. Mater. Chem. A. 3 (2015) 3480–

3490. doi:10.1039/C4TA06715K.

[54] T.K. Gupta, B.P. Singh, V.N. Singh, S. Teotia, A.P. Singh, I. Elizabeth, et al., MnO2 decorated graphene nanoribbons with superior permittivity and excellent microwave shielding properties, J. Mater. Chem. A. 2 (2014) 4256. doi:10.1039/c3ta14854h.

[55] K. Fic, G. Lota, M. Meller, E. Frackowiak, Novel insight into neutral medium as electrolyte for high-voltage supercapacitors, Energy Environ. Sci. 5 (2012) 5842–5850. doi:10.1039/C1EE02262H.

[56] Q. Gao, L. Demarconnay, E. Raymundo-Piñero, F. Béguin, Exploring the large voltage range of carbon/carbon supercapacitors in aqueous lithium sulfate electrolyte, Energy Environ. Sci. 5 (2012) 9611. doi:10.1039/c2ee22284a.

[57] A.N. Naveen, S. Selladurai, A 1-D/2-D hybrid nanostructured manganese cobaltite–graphene nanocomposite for electrochemical energy storage, RSC Adv. 5 (2015) 65139–65152. doi:10.1039/C5RA09288D.

[58] E. Frackowiak, Carbon materials for supercapacitor application, Phys. Chem. Chem. Phys. 9 (2007) 1774. doi:10.1039/b618139m.

[59] J.P. Cheng, L. Liu, J. Zhang, F. Liu, X.B. Zhang, Influences of anion exchange and phase transformation on the supercapacitive properties of α-Co(OH)2, J. Electroanal. Chem. 722–723 (2014) 23–31. doi:10.1016/j.jelechem.2014.03.019.

[60] L.-H.H. Su, X.-G.G. Zhang, Y. Liu, Electrochemical performance of Co-Al layered double hydroxide nanosheets mixed with multiwall carbon nanotubes, J. Solid State

Electrochem. 12 (2008) 1129–1134. doi:10.1007/s10008-007-0455-5.

[61] D. Pech, M. Brunet, H. Durou, P. Huang, V. Mochalin, Y. Gogotsi, et al., Ultrahigh-power micrometre-sized supercapacitors based on onion-like carbon, Nat. Nanotechnol. 5 (2010) 651–654.

[62] C. Masarapu, H.F. Zeng, K.H. Hung, B. Wei, Effect of temperature on the capacitance of carbon nanotube supercapacitors, ACS Nano. 3 (2009) 2199–2206.

[63] X. Liu, R. Ma, Y. Bando, T. Sasaki, A General Strategy to Layered Transition-Metal Hydroxide Nanocones: Tuning the Composition for High Electrochemical Performance, Adv. Mater. 24 (2012) 2148–2153. doi:10.1002/adma.201104753.

[64] S.I. Cordoba, R.E. Carbonio, M.L. Teijelo, V.A. Macagno, The electrochemical response of binary mixtures of hydrous transition metal hydroxides co-precipitated on conducting substrates with reference to the oxygen evolution reaction, Electrochim. Acta. 31 (1986) 1321–1332. doi:10.1016/0013-4686(86)80155-4.

[65] H. Guan, L.-Z. Fan, H. Zhang, X. Qu, Polyaniline nanofibers obtained by interfacial polymerization for high-rate supercapacitors, Electrochim. Acta. 56 (2010) 964–968.

[66] P.L. Taberna, P. Simon, J.-F.F. Fauvarque, Electrochemical Characteristics and Impedance Spectroscopy Studies of Carbon-Carbon Supercapacitors, J. Electrochem. Soc. 150 (2003) A292-300. doi:10.1149/1.1543948.

[67] Optimisation of an asymmetric manganese oxide/activated carbon capacitor working at 2 V in aqueous medium, J. Power Sources. 153 (2006) 183–190.

doi:10.1016/J.JPOWSOUR.2005.03.210.

[68] I.I. Misnon, R. Jose, Synthesis and electrochemical evaluation of the PANI/δ-MnO_2 electrode for high performing asymmetric supercapacitors, New J. Chem. 41 (2017) 6574–6584. doi:10.1039/C7NJ00679A.

[69] T. Cottineau, M. Toupin, T. Delahaye, T. Brousse, D. Bélanger, Nanostructured transition metal oxides for aqueous hybrid electrochemical supercapacitors, Appl. Phys. A. 82 (2006) 599–606. doi:10.1007/s00339-005-3401-3.

[70] Q. Qu, P. Zhang, B. Wang, Y. Chen, S. Tian, Y. Wu, et al., Electrochemical Performance of MnO_2 Nanorods in Neutral Aqueous Electrolytes as a Cathode for Asymmetric Supercapacitors, J. Phys. Chem. C. 113 (2009) 14020–14027. doi:10.1021/jp8113094.

[71] Z.-S. Wu, W. Ren, D.-W. Wang, F. Li, B. Liu, H.-M. Cheng, High-Energy MnO_2 Nanowire/Graphene and Graphene Asymmetric Electrochemical Capacitors, ACS Nano. 4 (2010) 5835–5842. doi:10.1021/nn101754k.

[72] Z. Fan, J. Yan, T. Wei, L. Zhi, G. Ning, T. Li, et al., Asymmetric Supercapacitors Based on Graphene/MnO2 and Activated Carbon Nanofiber Electrodes with High Power and Energy Density, Adv. Funct. Mater. 21 (2011) 2366–2375. doi:10.1002/adfm.201100058.

[73] H. Gao, F. Xiao, C.B. Ching, H. Duan, High-Performance Asymmetric Supercapacitor Based on Graphene Hydrogel and Nanostructured MnO_2, ACS Appl. Mater. Interfaces. 4 (2012) 2801–2810. doi:10.1021/am300455d.

[74] Y. Shao, H. Wang, Q. Zhang, Y. Li, High-performance flexible asymmetric supercapacitors

based on 3D porous graphene/MnO_2 nanorod and graphene/Ag hybrid thin-film electrodes, J. Mater. Chem. C. 1 (2013) 1245–1251. doi:10.1039/C2TC00235C.

[75] L. Peng, X. Peng, B. Liu, C. Wu, Y. Xie, G. Yu, Ultrathin Two-Dimensional MnO_2 /Graphene Hybrid Nanostructures for High-Performance, Flexible Planar Supercapacitors, Nano Lett. 13 (2013) 2151–2157. doi:10.1021/nl400600x.